Mixology of $MA_{1-x}EA_xPbI_3$ Hybrid Perovskites: Phase Transitions, Cation Dynamics and Photoluminescence

Mantas Šimėnas,[*,†] Sergejus Balčiūnas,[†] Anna Gągor,[‡] Agnieszka Pieniążek,[¶] Kasper Tolborg,[§] Martynas Kinka,[†] Vytautas Klimavicius,[‖] Šarūnas Svirskas,[†] Vidmantas Kalendra,[†] Maciej Ptak,[‡] Daria Szewczyk,[‡] Artur Herman,[¶] Robert Kudrawiec,[¶] Adam Sieradzki,[⊥] Robertas Grigalaitis,[†] Aron Walsh,[§] Mirosław Mączka,[‡] and Jūras Banys[†]

†*Faculty of Physics, Vilnius University, Sauletekio 3, LT-10257 Vilnius, Lithuania*

‡*Institute of Low Temperature and Structure Research, Polish Academy of Sciences, Okólna 2, 50-422, PL-50-422 Wroclaw, Poland*

¶*Department of Semiconductor Materials Engineering, Wroclaw University of Science and Technology, Wybrzeze Wyspianskiego 27, PL-50-370 Wroclaw, Poland*

§*Thomas Young Centre and Department of Materials, Imperial College London, SW7 2AZ London, United Kingdom*

‖*Institute of Chemical Physics, Vilnius University, Sauletekio 3, LT-10257 Vilnius, Lithuania*

⊥*Department of Experimental Physics, Wroclaw University of Science and Technology, Wybrzeze Wyspianskiego 27, PL-50-370 Wroclaw, Poland*

E-mail: mantas.simenas@ff.vu.lt

Abstract

Mixing of molecular cations in hybrid lead halide perovskites is a highly effective approach to enhance stability and performance of the optoelectronic devices based on these compounds. In this work, we prepare and study novel mixed methylammonium (MA)-ethylammonium (EA) $MA_{1-x}EA_xPbI_3$ ($x < 0.4$) hybrid perovskites. We use a suite of different techniques to determine the structural phase diagram, cation dynamics and photoluminescence properties of these compounds. Upon introduction of EA, we observe a gradual lowering of the phase transition temperatures indicating stabilization of the cubic phase. For mixing levels higher than 30%, we obtain a complete suppression of the low-temperature phase transition and formation of a new tetragonal phase with different symmetry. We use the broadband dielectric spectroscopy to study the dielectric response of the mixed compounds in an extensive frequency range, which allows us to distinguish and characterize three distinct dipolar relaxation processes related to the molecular cation dynamics. We observe that mixing increases the rotation barrier of the MA cations and tunes the dielectric permittivity values. For the highest mixing levels, we observe signatures of the dipolar glass phase formation. Our findings are supported by the density functional theory calculations. Our photoluminescence measurements reveal a small change of the band gap upon mixing indicating suitability of these compounds for optoelectronic applications.

Introduction

Hybrid methylammonium (MA, $CH_3NH_3^+$) lead halide perovskites $MAPbX_3$ (X = I, Br, Cl) are extensively investigated as efficient and solution-processable photovoltaic materials.[1,2] The power conversion efficiency of solar cells based on these compounds experienced an extraordinary boost in the last decade and currently exceeds 25%.[3–8] Several key physical properties such as large absorption coefficient,[9] optimal band gap,[10] long carrier diffusion length,[11,12] low exciton binding energy,[13] and defect tolerance[14] are responsible for the high performance of these materials. Some of these properties and thus the device operation

can be significantly affected by the dynamics of the molecular cations and structural phase transitions occurring in these compounds.[10,15–20]

The best performing photovoltaic devices based on hybrid perovskites are obtained using compositions with mixed A-site cations.[21,22] The most popular alternatives to MA are formamidinium (FA, $HC(NH_2)_2^+$)[7,8] and Cs^+,[23] although other such as ethylammoniumm (EA, $CH_3CH_2NH_3^+$),[24–29] dimethylammonium (DMA, $(CH_3)_2NH_2^+$),[30–32] methylhydrazinium (MHy, $CH_3NH_2NH_2^+$),[33,34] and Rb^+[35] are also becoming of great interest. In addition to improved performance, the cation mixing significantly increases the stability of lead halide perovskites.[22] For example, mixing prevents a spontaneous conversion of the desirable photoactive black phase of $FAPbI_3$ and $CsPbI_3$ to the photoinactive yellow phase.[36–38]

Despite many studies concentrating on the photovoltaic performance of mixed lead halide perovskites, mixing effects on the structural phases, phase transitions and cation dynamics are significantly less studied and understood. Previously, we investigated these phenomena in $MA_{1-x}DMA_xPbBr_3$[32] and $MA_{1-x}FA_xPbBr_3$[39] compounds revealing stabilization of the desirable cubic phase by suppression of the structural phase transitions. In addition, strong signatures of the electric dipole glass phase resulting from the frustrated MA cations were observed in $MA_{1-x}DMA_xPbBr_3$,[32] while this effect was weaker in $MA_{1-x}FA_xPbBr_3$ mixed system.[39] Indications of the dipolar glass phase were also previously observed in $MA_{1-x}Cs_xPbBr_3$[40] and $MA_{1-x}FA_xPbI_3$[41] mixtures.

In this work, we use a suite of experimental and theoretical techniques to study a promising novel mixed-cation $MA_{1-x}EA_xPbI_3$ perovskite system. The hybrid compounds containing EA cations are gaining significant attention for their improved stability and photovoltaic performance.[24–29,42–44] Pure $EAPbI_3$ crystallizes into the orthorhombic ($Pnma$) symmetry[45–47] with the anionic component having a 1D architecture composed of $[PbI_3]_n^-$ columns which are built of face-sharing octahedra, however no information is available on the structural phase transitions of this compound. The band gap of this compound is 2.2 eV making it suitable for photovoltaic applications.[45] In contrast, the phase transitions of pure $MAPbI_3$ are rather

well known: this compound exhibits two transitions at 327 and 162 K corresponding to the cubic ($Pm\bar{3}m$) $\rightarrow$ tetragonal ($I4/mcm$) $\rightarrow$ orthorhombic ($Pnma$) symmetry lowering followed by the MA cation ordering into a non-ferroelectric phase.[17,48–51]

This work reveals that mixing of $MAPbI_3$ with EA stabilizes the cubic phase, as the temperatures of both structural phase transitions are significantly reduced. For higher EA concentration, we obtain a complete suppression of the low-temperature phase transition and formation of a new tetragonal phase of different symmetry. Our broadband dielectric spectroscopy experiments of single crystal samples indicate signatures of a dipolar glass phase and a substantial perturbation of the MA cation dynamics. Our experimental results are supported by the density functional theory (DFT) calculations of the potential energy surface for molecular rotations. We also study the photoluminescence properties of these mixed compounds revealing a small change of the band gap upon mixing.

Experimental Details

Sample synthesis

Single crystals of $MA_{1-x}EA_xPbI_3$ were grown in a similar way as recently proposed by Fateev et al. for crystallization of $MAPbI_3$ and a number of 2D iodides.[52] During a typical synthesis, 4 mmol of PbI_2 and stoichiometric amounts of methylamine (2M solution in methanol, Sigma Aldrich) and ethylamine (2M solution in methanol, Sigma Aldrich) were added to a mixture of propylene carbonate (PC, 99.7%, Sigma-Aldrich) and HI (57 wt. % in H_2O, stabilized with H_3PO_2, Sigma-Aldrich) under stirring until a complete dissolution of the solids ($\sim$ 6 mL). The PC:HI volume ratio was 2.8:1, and the total amount of methylamine and ethylamine was 4 mmol. The clear solution was transferred into a glass vial with the lid slightly loosened. Then the vial was kept at 50°C for 2-3 days, and the grown black crystals with dimensions up to 5 mm were separated from the liquid and dried at room temperature. The crystals of $EAPbI_3$ were yellow up to 3 mm in size. The fraction x of the EA cations in $MA_{1-x}EA_xPbI_3$

compounds was determined using ^{1}H NMR spectroscopy.

NMR

^{1}H NMR experiments were carried out at 14.1 T on a Bruker Avance Neo NMR spectrometer operating at 600.3 MHz using a 5 mm Bruker ^{1}H - ^{13}C - BB TBI probe. Temperature was stabilized at 298 K. A pulse sequence employing 10 μs $\pi/6$ excitation pulse followed by 5 s repetition delay was employed, and 64 scans were accumulated. Samples were dissolved in DMSO-d_6 (99.96 % D atom, Sigma Aldrich) which was used for lock. For signal assignment, the ^{1}H$-^{1}$H COSY pulse sequence was employed by collecting 4 scans for 256 increments. The obtained NMR spectra and their analysis are presented in the Supporting Information.

Raman spectroscopy

Room temperature Raman spectra of polycrystalline samples were measured using a Bruker FT100/S spectrometer equipped with a YAG:Nd^{3+} laser excitation (1064 nm). The spectral resolution was set to 2 cm^{-1}.

Temperature-dependent Raman spectra of randomly oriented single crystals of $x = 0.38$ and $EAPbI_3$ samples were measured in the $1750 - 150$ cm^{-1} range using a Renishaw inVia Raman spectrometer with a confocal DM2500 Leica optical microscope, a thermoelectrically cooled CCD detector, and a diode laser operating at 830 nm. The low-wavenumber Raman spectra of $EAPbI_3$ ($200 - 20$ cm^{-1}) were obtained using the same setup but with an extra Eclipse filter. A THMS600 Temperature Control Stage for Microscopy (Linkam) was used for temperature control in all experiments.

Photoluminescence

Temperature-dependent photoluminescence spectra were obtained in a closed cycle cryostat allowing measurements from 20 to 300 K. The $x = 0.09$, $x = 0.16$, and $x = 0.21$ samples

were excited by a 532 nm line from a diode-pumped solid-state laser (power 500 µW), while a 405 nm laser (power 500 µW) was used to excite the $x = 0.38$ sample. Additionally, the photoluminescence spectra were excited by a 325 nm line from a HeCd laser. No significant differences in the photoluminescence spectra were observed for the three excitation wavelengths. Photoluminescence signals were collected using a Peltier-cooled Avantes CCD spectrometer.

DSC

The differential scanning calorimetry (DSC) experiments of powder samples were performed using a Mettler Toledo DSC-1 calorimeter with a resolution of 0.4 µW. Nitrogen was used as a purging gas, and the heating/cooling rate was 5 K/min. Mass of the samples (in mg): 75.85 ($x = 0$), 69.99 ($x = 0.09$), 47.43 ($x = 0.16$), 31.02 ($x = 0.21$), 32.00 ($x = 0.31$), 29.76 ($x = 0.38$), and 32.45 ($x = 1$).

Heat capacity

Heat capacity at constant pressure C_p of all samples was measured in the temperature range of 1.8-350 K using thermal relaxation technique in the heat capacity option of the physical property measurements system (PPMS). The typical accuracy of the system is better than 1% for temperatures above 100 K and slightly diminishes at lower temperatures. For the measurements, single crystal samples were used with a typical sample mass of about 6 mg.

Ultrasonic measurements

The ultrasonic velocity and attenuation data of single crystal samples were obtained from the phase shift and amplitude of the received signal using RITEC RAM-5000 pulse-echo ultrasonic measurement system. $LiNbO_3$ transducers were used for the excitation and detection of the longitudinal ultrasonic waves at 10 MHz. Typical sample thickness was 2-3

mm, and heating/cooling rate was kept below 1 K/min. Silicon oil was used between the sample, quartz buffer rods and transducers to maintain acoustic bonds in the whole studied temperature range.

XRD

The single crystal X-ray diffraction (XRD) data were collected on the four-circle Xcalibur diffractometer operating with Mo K-α radiation, CCD Atlas camera, and Oxford Diffraction cooling system. CrysAlisPro was used for the data processing (CrysAlis PRO 1.171.38.43 (Rigaku OD, 2015)). For the $x < 1$ samples, the lattice parameters were calculated for the archetype $Pm\bar{3}m$ cubic phase (using the orthorhombic restraints: all α, β, and γ angles were set to 90°).

Powder XRD (PXRD) measurements were performed on an X'Pert PRO powder diffractometer operating with Cu K-α radiation.

Dielectric spectroscopy

Broadband dielectric spectroscopy experiments of single crystal samples were performed in three different frequency bands. (i) 10 mHz–100 kHz band: measurements of capacitance and loss tangent with Solartron Modulab XM MTS system together with XM MFA low-current module (only $x = 0.38$ sample). (ii) 20 Hz–1 MHz band: measurements of capacitance and loss tangent with HP4284A LCR meter (all samples). In both cases, the flat capacitor model was implemented to calculate the complex dielectric permittivity. (iii) 1 MHz–1 GHz band: the complex reflection coefficient was measured with Agilent 8714ET vector network analyzer. The multimode capacitor model was used to calculate the complex dielectric permittivity.[53,54] Temperature-dependent dielectric spectra were measured on cooling at a rate of 1 K/min. In all cases, silver paste was used for sample electrodes. Temperature was measured with a Keithley Integra 2700 multimeter, a T-type thermocouple and a 100 Ω platinum resistor. For measurements at low frequency (10 mHz–100 kHz band), the tem-

perature was stabilized before performing the experiment. The uncertainty of the sample size and imperfect calibration of the measurement setups results in about 3% error of the determined dielectric permittivity.

DFT calculations

The $MA_{0.875}EA_{0.125}PbI_3$ mixed cation perovskite was simulated using DFT in the Vienna Ab Initio Simulation (VASP) code.[55] A $2 \times 2 \times 2$ supercell in the settings of the parent cubic perovskite $MAPbI_3$ was generated from the orthorhombic structure of $MAPbI_3$, and all coordinates and cell parameters were relaxed. One of the eight MA cations was substituted with EA and fully relaxed. Several initial EA orientations within the same framework of MA orientations were tried, and the lowest energy one was selected for further modelling. Rotation barriers were constructed from rigid rotation of the molecular cations around their center of mass. The DFT calculations were performed with a planewave cutoff of 550 eV, a $4 \times 4 \times 4$ Γ-centred k-points mesh, PAW pseudopotentials,[56] and the PBEsol exchange-correlation functional.[57]

Results and Discussion

We studied $MA_{1-x}EA_xPbI_3$ perovskite crystals with the EA fraction of $x = 0$, 0.09, 0.16, 0.21, 0.31, 0.38, and 1, where x was determined by ^{1}H NMR spectroscopy (see Figures S1 and S2, Supplementary Information). We were not able to obtain the intermediate mixing levels ($x > 0.4$) indicating the EA solubility limit in $MAPbI_3$ of about 40%, which is in a close agreement with the result reported by Wang et al.[58] A subsequent sample characterization using room-temperature Raman spectroscopy also revealed a monotonous increase of the EA band intensity with increasing EA content (Figure S3), while the PXRD patterns exhibited no reflections of the secondary or unmixed phases (Figure S7). These experiments demonstrate a successful incorporation of the EA cations in these compounds.

To study the behaviour of the structural phase transitions of $MA_{1-x}EA_xPbI_3$, we used a suite of different experimental techniques including measurements of the heat capacity C_p, DSC, ultrasonic propagation, dielectric properties, Raman spectroscopy, and single-crystal XRD. Such a combination of tools proved to be highly successful in distinguishing phase transition anomalies from the experimental artefacts as demonstrated by our previous studies on other mixed hybrid perovskite systems.[32,39]

The measured C_p, DSC (Figure 1) and ultrasonic (Figure S8) data revealed two structural phase transitions of $MAPbI_3$ ($x = 0$) at 329 and 161 K in agreement with previous reports.[17,48,50,51] Upon increase of the EA fraction, we observed a gradual lowering of both transition temperatures indicating stabilization of the desirable cubic phase. A similar behaviour was also observed for the related mixed hybrid perovskites.[32,39,41]

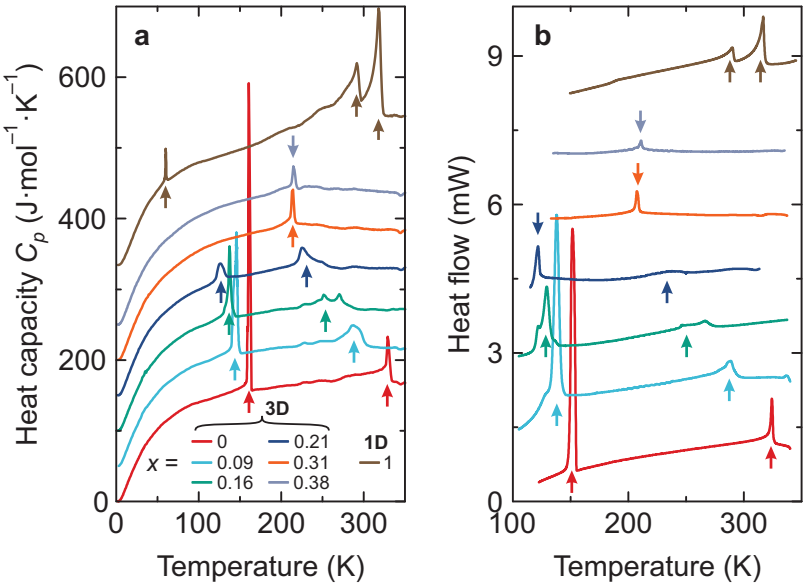

Figure 1: Temperature dependence of the (a) heat capacity and (b) DSC traces of $MA_{1-x}EA_xPbI_3$ perovskites. The curves are offset by an arbitrary shift for clarity. The arrows indicate phase transition anomalies.

At higher concentration of EA ($x = 0.31$ and 0.38), the low-temperature transition becomes completely suppressed (see Figures 1, S5, S8 and S9). Interestingly, the anomaly of the remaining transition is sharper compared to the lower EA concentrations. Our single crystal XRD experiments also show that the space group of the $x = 0.31$ and 0.38 samples is no

longer body-centered, but instead can be described by a primitive tetragonal or pseudotetragonal (with very weak orthorhombic deformation) symmetry (see Supporting Information). However, a reliable solution of the crystal structure of these compounds is beyond the resolution of our currently accessible methods. We performed temperature-dependent Raman experiments to infer the low-temperature ordering of the $x = 0.38$ compound. Our experiments revealed that the Raman bands at 80 K of this sample are significantly wider compared to the nonmixed $EAPbI_3$ (see Figures S4 and S6) or low-temperature structures of $MAPbI_3$ and $MAPbBr_3$[59,60] indicating a substantial disorder related to the molecular cations even at low temperature. In particular, the tetragonal to orthorhombic phase transition in $MAPbI_3$ and $MAPbBr_3$ leads to drastic narrowing of the Raman bands near 1590 and 920 cm^{-1},[59,60] which is not observed for the $x = 0.38$ indicating lack of the MA ordering. We summarized the obtained results in the temperature-concentration phase diagram presented in Figure 2a.

We also performed the same type of experiments to study previously unknown structural phase transitions of $EAPbI_3$, which crystallizes into a 1D perovskite structure.[47] Our measurements revealed three phase transition anomalies at 320, 292 and 60 K (Figures 1, S5, S8, S11). Interestingly, a transition at such a low temperature of 60 K is unusual for hybrid perovskites and related compounds and was never observed before.[20] We used XRD experiments to study the symmetry lowering during the high-temperature transitions (see Supporting Information) and obtained the hexagonal ($P6_3/mmc$) $\rightarrow$ orthorhombic ($Pnma$) $\rightarrow$ monoclinic ($P2_1/c$) decrease of symmetry on cooling (summarized in Figure 2a). Note that we did not study the low-temperature phase of $EAPbI_3$, as the phase transition at 60 K is outside the temperature range accessible by our XRD equipment.

We further performed broadband dielectric spectroscopy experiments on the single crystal samples to investigate the molecular cation dynamics in the different regions of the phase diagram. The temperature dependence of the real ε' and imaginary ε'' (dielectric loss) parts of the complex dielectric permittivity $\varepsilon^* = \varepsilon' - i\varepsilon''$ for all studied compositions is presented in Figure 3. For the $x = 0$ sample, ε^* shows a sudden decrease at the

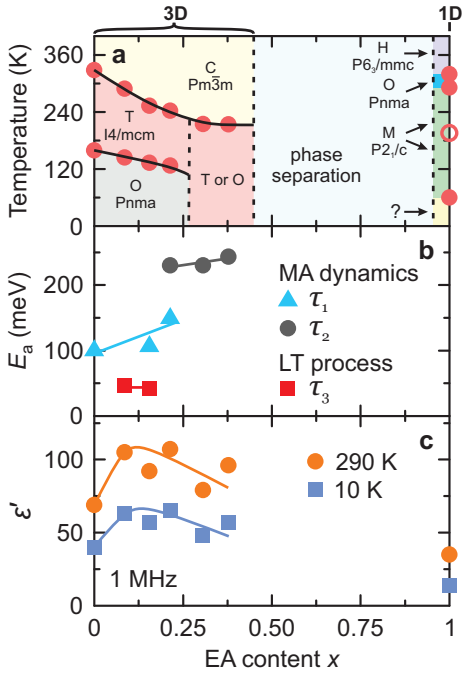

Figure 2: (a) Temperature-composition phase diagram of mixed $MA_{1-x}EA_xPbI_3$ perovskite. The filled dots indicate structural phase transitions, while the empty dot marks the isostructural dielectric anomaly of $EAPbI_3$. The dashed curves indicate tentative phase boundaries. Abbreviations: C - cubic, T - tetragonal, O - orthorhombic, H - hexagonal, M - monoclinic. (b) EA concentration dependence of the activation energy of the MA cation dynamics and the low-temperature process. (c) $\varepsilon'(1\ \mathrm{MHz})$ vs. x obtained at 290 and 10 K. The solid curves are guides for the eye. The error bars are smaller than data points.

tetragonal-orthorhombic phase transition point, which is caused by the cooperative ordering of the MA electric dipoles.[17,32,39,41,61–63] Upon mixing with the EA cations, the temperature of this anomaly decreases with increasing x (Figure 3b-d) in agreement with other experiments. For the highest mixing levels, the phase transition disappears transforming to a broad dipolar relaxation (Figure 3e,f). This indicates a substantial disorder at low temperature in agreement with the Raman spectroscopy results. Interestingly, for the $x = 0$ sample, the cubic-tetragonal phase transition exhibits no dielectric anomaly (Figure S11), but for the mixed compounds this transition becomes clearly visible in the low-frequency dielectric response (Figure 3b-f).

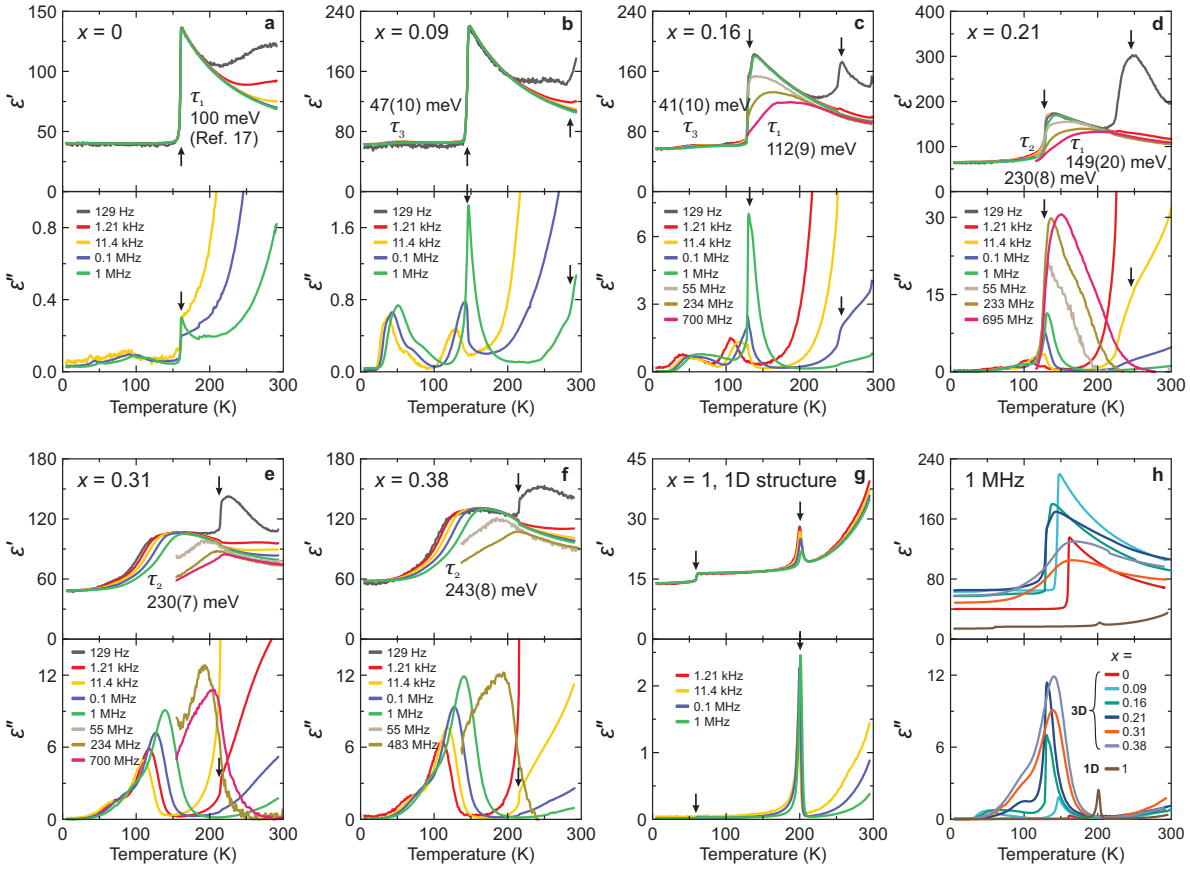

Figure 3: (a-g) Temperature dependence of the complex dielectric permittivity of $MA_{1-x}EA_xPbI_3$ single crystals presented at selected frequencies. The arrows indicate phase transition anomalies. Different relaxation processes (τ_1, τ_2 and τ_3) are indicated together with the determined activation energies. (h) Comparison of the complex dielectric permittivity obtained at 1 MHz for all studied compositions.

We also studied the dielectric properties of the nonmixed $EAPbI_3$ compound (Figures 3g and S11). In addition to the aforementioned three phase transitions, we also observed a strong additional anomaly at about 190 K. Our XRD experiments revealed no associated symmetry change, which may indicate an isostructural character of this transition associated with the electric dipoles. A small anomaly at this temperature also appears in the Raman data (Figure S5). Note that such symmetry-preserving transitions are rather frequent in hybrid perovskites and related materials.[19,39,64]

Our dielectric experiments also allowed us to capture and distinguish different dipolar relaxation processes in the studied compounds. Based on the previous studies, the rotational dynamics of the MA cations in the tetragonal phase of $MAPbI_3$ occur in the GHz frequency range[65] with the activation (barrier) energy E_a of 100 meV.[17] We refer to this process as τ_1. We performed sufficiently broadband experiments for the $x = 0.16$ and 0.21 samples revealing presence of this process (Figure 3c,d), while the analysis of the frequency domain data (see Supporting Information) allowed to determine the E_a values: 112(9) meV ($x = 0.16$) and 149(20) meV ($x = 0.21$). This indicates that the MA rotation barrier increases with the increasing concentration of the EA cations as is also summarized in Figure 2b. A similar trend and activation energies were also observed for other mixed perovskite systems[32,39] indicating a universal hindering of the MA motion upon mixing.

Due to the disappearance of the low-temperature transition in the highly mixed compounds ($x = 0.31$ and 0.38), the main dipolar relaxation extends to much lower temperatures (Figure 3e,f), and we refer to this process as τ_2. Despite looking very similar to τ_1, this relaxation has much higher activation energy of $E_a > 200$ meV (Figures 2b and S13). Together with the complete suppression of the phase transition, this observation indicates a qualitatively different behaviour of the molecular cations in this highly mixed region of the phase diagram. Note that this process is also very weakly visible just below the tetragonal-orthorhombic phase transition for the $x = 0.21$ sample (Figure 3d) suggesting that this concentration is somewhat intermediate between the two regimes.

Such a broad dipolar relaxation of the highly mixed compounds may indicate that the MA cations form a dipolar glass phase due to the dipole frustration introduced by mixing, which is frequently observed in mixed inorganic compounds.[66–69] However, here we did not observe a clear Vogel-Fulcher behaviour of the mean relaxation time despite our broadband (Hz-GHz) approach, as the Arrhenius law was sufficient to describe the obtained data (Figure S13). Observation of the Vogel-Fulcher law would indicate freezing of the electric dipoles and would provide an unequivocal evidence of such a phase formation.[67,68] The absence of this behaviour suggests that the freezing might occur at very low temperatures. Note that similar hints to the glassy phase formation were also observed in the dielectric responses of the related $MA_{1-x}DMA_xPbBr_3$ (strong signatures)[32] and $MA_{1-x}FA_xPbBr_3$ (weaker signatures)[39] systems.

A third dipolar relaxation (τ_3) we observed occurs in the weakly mixed compounds ($x \leq 0.16$) at low temperature (< 100 K) (Figure 3b,c). The strength of this process and activation energy (around 45 meV, Figure 2b) are much smaller compared to the τ_1 and τ_2 processes. There are also some indications of this process occurring in the nonmixed $MAPbI_3$, but we were not able to reliable extract the E_a value for this sample. Fabini et al.[61] also detected a similar low-temperature relaxation for the $MAPbI_3$ compound and assigned it to dynamics of a glassy phase. On the other hand, Xu et al.[70] used magnetic resonance to observe that the MA cations in $MAPbI_3$ undergo twisting in the orthorhombic phase with the activation energy of 60 meV, which is rather close to the energy of the τ_3 process determined from our experiments. As formation of a glassy phase in nonmixed $MAPbI_3$ compound is less likely, the second explanation seems more plausible.

EA cations also affect the value of the dielectric permittivity of $MA_{1-x}EA_xPbI_3$ (Figures 2c and 3). For small x, ε' seems to slightly increase with increasing x, while for higher mixing levels it decreases suggesting hindered dynamics of the MA cations. Note that the dielectric permittivity of the nonmixed $EAPbI_3$ is much smaller compared to the mixed structures (Figure 3g,h). The value of ε' obtained at 10 K, where cation relaxations are

absent, is about 50 for all studied compounds except for $EAPbI_3$ ($\varepsilon' \sim 15$). Similar values of the low-temperature dielectric permittivity were also obtained for other mixed lead halide perovskites.[32,39] As discussed by Fabini,[71] such a universal and rather high value of the dielectric permittivity is related to the lattice polarizability invoked by the $6s^2$ lone-pair electrons and associated off-centering of the lead cations.

To gain insights on the microscopic picture of the mixing and to support our dielectric data, we performed DFT calculations on a mixed $MA_{0.875}EA_{0.125}PbI_3$ supercell based on the orthorhombic structure of $MAPbI_3$ (Figure 4a). Our calculations show that the long molecular axis (dipole moment) of the EA cation is approximately along the $< 100 >$-family of crystal directions. A rotation potential was constructed by rotating the EA and the nearest-neighbour MA cation around three orthogonal lattice directions (Figure 4b). The obtained results indicate that the rotation barriers for the EA cations are about two times higher compared to the MA cations, except for the rotation axis, which coincides with the dipole moment of the EA cation and thus preserves its orientation. This strongly supports our claims that the dominant dielectric response originates from the MA cations.

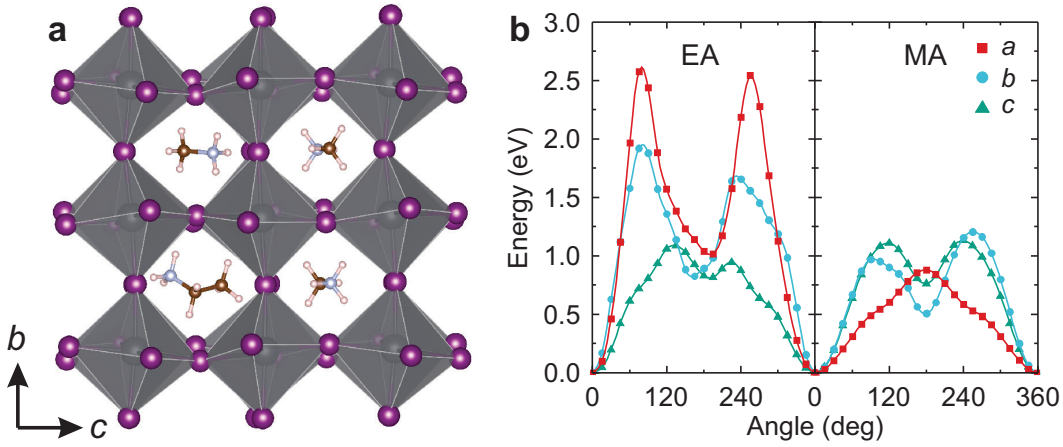

Figure 4: (a) Relaxed DFT structure of $MA_{0.875}EA_{0.125}PbI_3$ used to calculate the rotation barriers of (b) the EA and the nearest-neighbour MA cation. For clarity, only a $2 \times 2 \times 1$ slab containing the EA cation is presented. The curves are guides for eye.

We also used DFT calculations to assess the differences in the rotation barriers for crystallographycally different MA cations in the $MA_{0.875}EA_{0.125}PbI_3$ supercell. Our results indicate

about 20% of variation in the rotational energies (see Figure S14) indicating that the dynamics of the MA cations are affected by the local lattice strains introduced by much bigger EA cations.[32] It is likely that for a higher EA concentration, the MA rotation barriers would experience even stronger perturbations leading to a glassy behaviour. Unfortunately, such DFT calculations would be very expensive necessitating a different computational approach such as molecular dynamics.

Finally, we also studied how cation mixing affects the optical properties of $MA_{1-x}EA_xPbI_3$ compounds. Figure 5 shows the normalized temperature-dependent photoluminescence spectra of the $x = 0.09, 0.16, 0.21$ and 0.38 samples obtained under the same excitation conditions. For lower EA concentrations, two photoluminescence peaks of comparable amplitudes (low-energy (LE) and high-energy (HE)) can be clearly distinguished at room temperature, while the LE peak is significantly weaker for the highest mixing level. In general, the LE peak in hybrid perovskites may be attributed to bound excitons and defect states, while free excitons cause the HE emission.[46,72,73]

The temperature dependences of the HE and LE peak positions are indicated in Figure 5e-h showing that the photoluminescence response is affected by the symmetry changes associated with the structural phase transitions. For the $x = 0.09, 0.16$ and 0.21 samples, the LE peak seems to have the same nature in the cubic and tetragonal phases, while the temperature dependence is significantly different in the orthorhombic phase. The $x = 0.38$ compound exhibits negligible changes of the photoluminescence response at the phase transition point adding evidence for a different behaviour of this highly mixed compound.

The comparison of the photoluminescence spectra and their decomposition into individual peaks (see Figure S15) revealed that the energy of the free exciton transition at room temperature slightly increases with increasing EA concentration and reaches saturation for the highest mixing level (Figure 5i). This can be attributed to widening of the band gap due to alloying with $EAPbI_3$, which has a larger band gap,[45] although changes of the exciton binding energy may also play a role. A slight increase of the bang gap of $MA_{1-x}EA_xPbI_3$

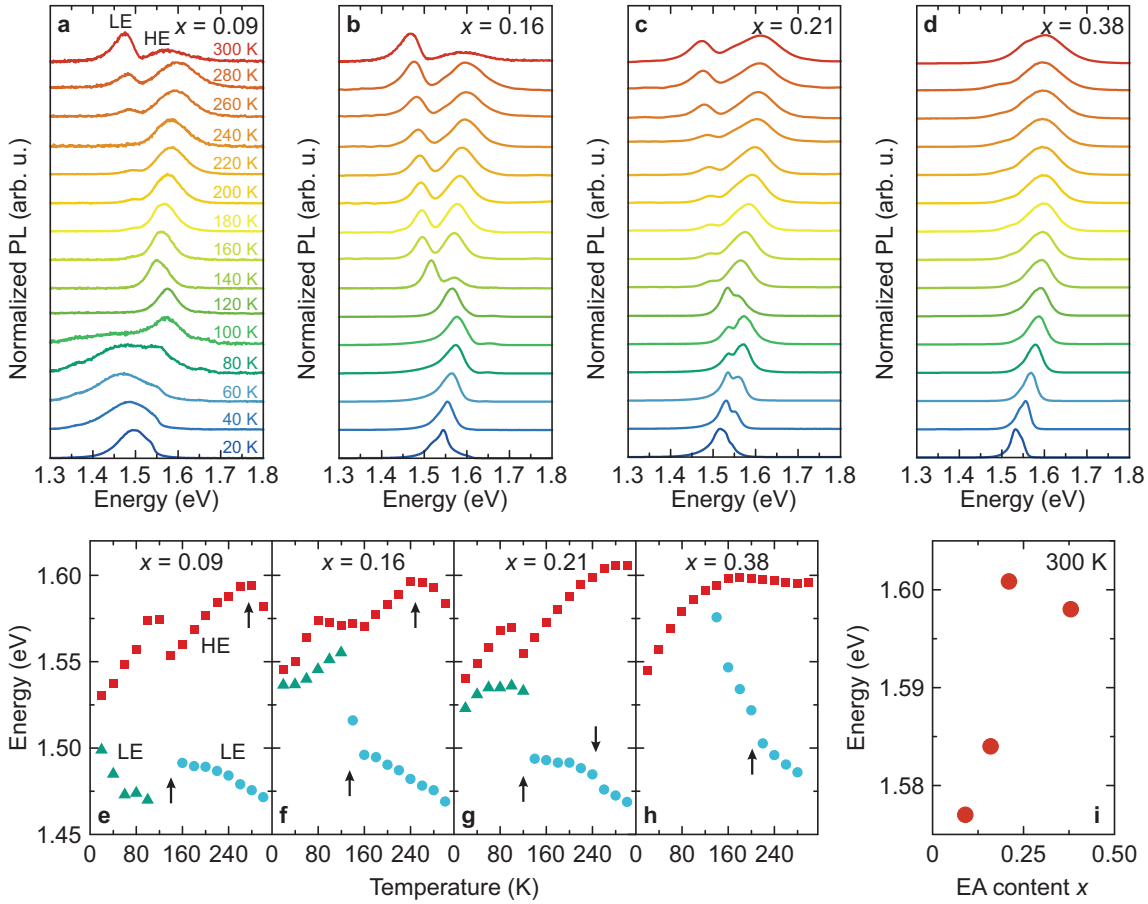

Figure 5: (a-d) Normalized photoluminescence spectra of $MA_{1-x}EA_xPbI_3$ perovskites measured at different temperatures on cooling. (e-h) Temperature dependence of the LE and HE peak energies. The arrows indicate phase transition points. (i) Energy of the free exciton emission at 300 K as a function of the EA content. The error bars are smaller than data points.

with increasing x was also recently predicted by Liu et al.[42]

Summary and Conclusions

We used a suite of different techniques to thoroughly study the structural phase transitions, phase diagram, cation dynamics, optical properties and broadband dielectric response of mixed cation $MA_{1-x}EA_xPbI_3$ hybrid perovskites. Understanding all these aspects is highly important for a successful applicability of novel EA-containing mixed hybrid perovskites in optoelectronics.

Our C_p, DSC and ultrasound experiments revealed a gradual lowering of the phase transition temperatures upon mixing indicating stabilization of the cubic phase. For higher mixing levels ($x \gtrsim 0.3$), we observed a complete suppression of the low-temperature phase transition, while the XRD experiments revealed that in this highly-mixed region the crystal symmetry changes from body-centered tetragonal to primitive tetragonal or weakly orthorhombic. Further studies involving more precise diffraction methods are necessary to probe this phase in more detail. As recently discussed by Huang et al. for the related $MA_{0.13}EA_{0.87}PbBr_3$ perovskite,[44] the disappearance of the low-temperature phase transition may be also related to the tolerance factor approaching unity upon mixing, which prevents large octahedral tilts associated with the orthorhombic *Pnma* phase. Upon further increase of x, we observed phase separation indicating that the EA solubility limit in $MAPbI_3$ is about 40%.

We used the broadband dielectric spectroscopy to study the molecular cation dynamics and dielectric properties of single crystal compounds. Depending on a mixing level, three distinct dipolar relaxations were observed. For small x, the main relaxation occurs in the tetragonal phase, which we attribute to the rotational dynamics of the MA cations. Upon increase of the EA content, the activation energy of this process increases indicating that the lattice deformation caused by the EA cations hinders the rotations of the MA cations. In the orthorhombic phase, a much weaker process is observed, which might be assigned to

the twisting motion of the MA cations.

At the highest mixing levels ($x = 0.21$ and 0.38), we observed a broad dipolar relaxation extending to very low temperatures with a significantly higher activation energy compared to the weakly mixed compounds. Such a relaxation indicates disordered phase and resembles a dipolar glass behaviour. A very similar dipolar relaxation was also observed for other mixed hybrid perovskites[32,39] indicating a common behaviour upon mixing, especially with the cations that cause a strong lattice distortion.

We also observed a substantial decrease of the dielectric permittivity value upon mixing, which might be related to much higher rotation barriers of the EA cations. The low-temperature permittivity value remains rather high ($\varepsilon' \sim 50$) indicating lattice polarizability by the lonepair electrons of the lead cations,[71] which also seems to be a universal behaviour of the lead-based hybrid perovskites.

We supported our dielectric spectroscopy results with the DFT calculations of the moderately mixed $x = 0.125$ compound, which revealed that the rotation barriers of the EA cation are much higher compared to the smaller MA cations indicating that the dominant dielectric response originates from the latter cations. Our calculations also indicate a considerable distribution of the MA cation rotation energies due to the local lattice strains introduced by the EA cations. This provides a microscopic mechanism behind the signatures of the glassy phase observed at the highest mixing levels.

Our temperature-dependent photoluminescence experiments revealed two emissions around 1.5 eV, which we attribute to the free and bound excitons. Both photoluminescence peaks are rather weakly affected by the structural phase transitions occurring in these compounds. We also observed a small increase of the emission energy of the free exciton with the increasing EA content, which we attribute to the widening of the band gap.

Supporting Information

Additional NMR, Raman, ultrasonic, XRD, dielectric, DFT and photoluminescence data.

Acknowledgement

This project has been funded by the Research Council of Lithuania (LMTLT) (agreement No. S-MIP-22-73). K.T. acknowledges the Independent Research Fund Denmark for funding through the International Postdoctoral grant (0164-00015B). Via our membership of the UK's HEC Materials Chemistry Consortium, which is funded by EPSRC (EP/L000202), this work used the ARCHER2 UK National Supercomputing Service (http://www.archer2.ac.uk).

References

(1) Snaith, H. J. Perovskites: The Emergence of a New Era for Low-Cost, High-Efficiency Solar Cells. *J. Phys. Chem. Lett.* **2013**, *4*, 3623–3630.

(2) Grätzel, M. The Light and Shade of Perovskite Solar Cells. *Nat. Mater.* **2014**, *13*, 838–842.

(3) Kojima, A.; Teshima, K.; Shirai, Y.; Miyasaka, T. Organometal Halide Perovskites as Visible-Light Sensitizers for Photovoltaic Cells. *J. Am. Chem. Soc.* **2009**, *131*, 6050–6051.

(4) Liu, M.; Johnston, M. B.; Snaith, H. J. Efficient Planar Heterojunction Perovskite Solar Cells by Vapour Deposition. *Nature* **2013**, *501*, 395–398.

(5) Park, N.-G. Organometal Perovskite Light Absorbers Toward a 20% Efficiency Low-Cost Solid-State Mesoscopic Solar Cell. *J. Phys. Chem. Lett.* **2013**, *4*, 2423–2429.

(6) Li, Z.; Klein, T. R.; Kim, D. H.; Yang, M.; Berry, J. J.; van Hest, M. F. A. M.; Zhu, K. Scalable Fabrication of Perovskite Solar Cells. *Nat. Rev. Mater.* **2018**, *3*, 18017 EP.

(7) Jeong, J.; Kim, M.; Seo, J.; Lu, H.; Ahlawat, P.; Mishra, A.; Yang, Y.; Hope, M. A.; Eickemeyer, F. T.; Kim, M. et al. Pseudo-Halide Anion Engineering for α-$FAPbI_3$ Perovskite Solar Cells. *Nature* **2021**, *592*, 381–385.

(8) Yoo, J. J.; Seo, G.; Chua, M. R.; Park, T. G.; Lu, Y.; Rotermund, F.; Kim, Y.-K.; Moon, C. S.; Jeon, N. J.; Correa-Baena, J.-P. et al. Efficient Perovskite Solar Cells via Improved Carrier Management. *Nature* **2021**, *590*, 587–593.

(9) Manser, J. S.; Christians, J. A.; Kamat, P. V. Intriguing Optoelectronic Properties of Metal Halide Perovskites. *Chem. Rev.* **2016**, *116*, 12956–13008.

(10) Frost, J. M.; Butler, K. T.; Brivio, F.; Hendon, C. H.; van Schilfgaarde, M.; Walsh, A. Atomistic Origins of High-Performance in Hybrid Halide Perovskite Solar Cells. *Nano Lett.* **2014**, *14*, 2584–2590.

(11) Stranks, S. D.; Eperon, G. E.; Grancini, G.; Menelaou, C.; Alcocer, M. J. P.; Leijtens, T.; Herz, L. M.; Petrozza, A.; Snaith, H. J. Electron-Hole Diffusion Lengths Exceeding 1 Micrometer in an Organometal Trihalide Perovskite Absorber. *Science* **2013**, *342*, 341–344.

(12) Chen, T.; Chen, W.-L.; Foley, B. J.; Lee, J.; Ruff, J. P. C.; Ko, J. Y. P.; Brown, C. M.; Harriger, L. W.; Zhang, D.; Park, C. et al. Origin of Long Lifetime of Band-Edge Charge Carriers in Organic-Inorganic Lead Iodide Perovskites. **2017**, *114*, 7519–7524.

(13) Miyata, A.; Mitioglu, A.; Plochocka, P.; Portugall, O.; Wang, J. T.-W.; Stranks, S. D.; Snaith, H. J.; Nicholas, R. J. Direct Measurement of the Exciton Binding Energy and Effective Masses for Charge Carriers in Organic-Inorganic Tri-Halide perovskites. *Nat. Phys.* **2015**, *11*, 582.

(14) Ball, J. M.; Petrozza, A. Defects in Perovskite-Halides and their Effects in Solar Cells. *Nat. Energy* **2016**, *1*, 16149.

(15) Frost, J. M.; Walsh, A. What Is Moving in Hybrid Halide Perovskite Solar Cells? *Accounts of Chemical Research* **2016**, *49*, 528–535.

(16) Egger, D. A.; Rappe, A. M.; Kronik, L. Hybrid Organic-Inorganic Perovskites on the Move. *Accounts of Chemical Research* **2016**, *49*, 573–581.

(17) Anusca, I.; Balčiūnas, S.; Gemeiner, P.; Svirskas, S.; Sanlialp, M.; Lackner, G.; Fettkenhauer, C.; Belovickis, J.; Samulionis, V.; Ivanov, M. et al. Dielectric Response: Answer to Many Questions in the Methylammonium Lead Halide Solar Cell Absorbers. *Adv. Energy Mater.* **2017**, *7*, 1700600.

(18) Herz, L. M. How Lattice Dynamics Moderate the Electronic Properties of Metal-Halide Perovskites. *J. Phys. Chem. Lett.* **2018**, *9*, 6853–6863.

(19) Mozur, E. M.; Trowbridge, J. C.; Maughan, A. E.; Gorman, M. J.; Brown, C. M.; Prisk, T. R.; Neilson, J. R. Dynamical Phase Transitions and Cation Orientation-Dependent Photoconductivity in $CH(NH_2)_2PbBr_3$. *ACS Mater. Lett.* **2019**, *1*, 260–264.

(20) Ptak, M.; Sieradzki, A.; Šimėnas, M.; Maczka, M. Molecular Spectroscopy of Hybrid Organic-Inorganic Perovskites and Related Compounds. *Coord. Chem. Rev.* **2021**, *448*, 214180.

(21) Zhou, Y.; Zhou, Z.; Chen, M.; Zong, Y.; Huang, J.; Pang, S.; Padture, N. P. Doping and Alloying for Improved Perovskite Solar Cells. *J. Mater. Chem. A* **2016**, *4*, 17623–17635.

(22) Ono, L. K.; Juarez-Perez, E. J.; Qi, Y. Progress on Perovskite Materials and Solar Cells with Mixed Cations and Halide Anions. *ACS Appl. Mater. Interfaces* **2017**, *9*, 30197–30246.

(23) Yao, H.; Zhao, J.; Li, Z.; Ci, Z.; Jin, Z. Research and Progress of Black Metastable Phase $CsPbI_3$ Solar Cells. *Mater. Chem. Front.* **2021**, *5*, 1221–1235.

(24) Hsu, H.-L.; Chang, C.-C.; Chen, C.-P.; Jiang, B.-H.; Jeng, R.-J.; Cheng, C.-H. High-Performance and High-Durability Perovskite Photovoltaic Devices Prepared using Ethylammonium Iodide as an Additive. *J. Mater. Chem. A* **2015**, *3*, 9271–9277.

(25) Peng, W.; Miao, X.; Adinolfi, V.; Alarousu, E.; El Tall, O.; Emwas, A.-H.; Zhao, C.; Walters, G.; Liu, J.; Ouellette, O. et al. Engineering of $CH_3NH_3PbI_3$ Perovskite Crystals by Alloying Large Organic Cations for Enhanced Thermal Stability and Transport Properties. *Angew. Chem. Int. Ed.* **2016**, *55*, 10686–10690.

(26) Shi, Z.; Zhang, Y.; Cui, C.; Li, B.; Zhou, W.; Ning, Z.; Mi, Q. Symmetrization of the Crystal Lattice of $MAPbI_3$ Boosts the Performance and Stability of Metal-Perovskite Photodiodes. *Adv. Mater.* **2017**, *29*, 1701656.

(27) Wu, C.; Chen, K.; Guo, D. Y.; Wang, S. L.; Li, P. G. Cations Substitution Tuning Phase Stability in Hybrid Perovskite Single Crystals by Strain Relaxation. *RSC Adv.* **2018**, *8*, 2900–2905.

(28) Nishi, K.; Oku, T.; Kishimoto, T.; Ueoka, N.; Suzuki, A. Photovoltaic Characteristics of $CH_3NH_3PbI_3$ Perovskite Solar Cells Added with Ethylammonium Bromide and Formamidinium Iodide. *Coatings* **2020**, *10*, 410.

(29) Kim, M.; Figueroa-Tapia, J. M.; Prato, M.; Petrozza, A. Engineering Multiphase Metal Halide Perovskites Thin Films for Stable and Efficient Solar Cells. *Adv. Energy Mater.* **2020**, *10*, 1903221.

(30) Pei, Y.; Liu, Y.; Li, F.; Bai, S.; Jian, X.; Liu, M. Unveiling Property of Hydrolysis-Derived $DMAPbI_3$ for Perovskite Devices: Composition Engineering, Defect Mitigation, and Stability Optimization. *iScience* **2019**, *15*, 165–172.

(31) Anelli, C.; Chierotti, M. R.; Bordignon, S.; Quadrelli, P.; Marongiu, D.; Bongiovanni, G.; Malavasi, L. Investigation of Dimethylammonium Solubility in $MAPbBr_3$ Hybrid Perovskite: Synthesis, Crystal Structure, and Optical Properties. *Inorg. Chem.* **2019**, *58*, 944–949.

(32) Šimėnas, M.; Balciunas, S.; Wilson, J. N.; Svirskas, S.; Kinka, M.; Garbaras, A.; Kalendra, V.; Gagor, A.; Szewczyk, D.; Sieradzki, A. et al. Suppression of Phase Transitions and Glass Phase Signatures in Mixed Cation Halide Perovskites. *Nat. Commun.* **2020**, *11*, 5103.

(33) Maczka, M.; Ptak, M.; Gagor, A.; Stefanska, D.; Zareba, J. K.; Sieradzki, A. Methylhydrazinium Lead Bromide: Noncentrosymmetric Three-Dimensional Perovskite with Exceptionally Large Framework Distortion and Green Photoluminescence. *Chem. Mater.* **2020**, *32*, 1667–1673.

(34) Maczka, M.; Gagor, A.; Zareba, J. K.; Stefanska, D.; Drozd, M.; Balciunas, S.; Šimėnas, M.; Banys, J.; Sieradzki, A. Three-Dimensional Perovskite Methylhydrazinium Lead Chloride with Two Polar Phases and Unusual Second-Harmonic Generation Bistability above Room Temperature. *Chem. Mater.* **2020**, *32*, 4072–4082.

(35) Saliba, M.; Matsui, T.; Domanski, K.; Seo, J.-Y.; Ummadisingu, A.; Zakeeruddin, S. M.; Correa-Baena, J.-P.; Tress, W. R.; Abate, A.; Hagfeldt, A. et al. Incorporation of Rubidium Cations Into Perovskite Solar Cells Improves Photovoltaic Performance. *Science* **2016**, *354*, 206–209.

(36) Jeon, N. J.; Noh, J. H.; Yang, W. S.; Kim, Y. C.; Ryu, S.; Seo, J.; Seok, S. I. Compositional Engineering of Perovskite Materials for High-Performance Solar Cells. *Nature* **2015**, *517*, 476 EP.

(37) Binek, A.; Hanusch, F. C.; Docampo, P.; Bein, T. Stabilization of the Trigonal High-

Temperature Phase of Formamidinium Lead Iodide. *J. Phys. Chem. Lett.* **2015**, *6*, 1249–1253.

(38) Charles, B.; Dillon, J.; Weber, O. J.; Islam, M. S.; Weller, M. T. Understanding the Stability of Mixed A-Cation Lead Iodide Perovskites. *J. Mater. Chem. A* **2017**, *5*, 22495–22499.

(39) Šimėnas, M.; Balciunas, S.; Svirskas, S.; Kinka, M.; Ptak, M.; Kalendra, V.; Gagor, A.; Szewczyk, D.; Sieradzki, A.; Grigalaitis, R. et al. Phase Diagram and Cation Dynamics of Mixed $MA_{1-x}FA_xPbBr_3$ Hybrid Perovskites. *Chem. Mater.* **2021**, *33*, 5926–5934.

(40) Mozur, E. M.; Maughan, A. E.; Cheng, Y.; Huq, A.; Jalarvo, N.; Daemen, L. L.; Neilson, J. R. Orientational Glass Formation in Substituted Hybrid Perovskites. *Chem. Mater.* **2017**, *29*, 10168–10177.

(41) Mohanty, A.; Swain, D.; Govinda, S.; Row, T. N. G.; Sarma, D. D. Phase Diagram and Dielectric Properties of $MA_{1-x}FA_xPbI_3$. *ACS Energy Lett.* **2019**, *4*, 2045–2051.

(42) Liu, D.; Li, Q.; Wu, K. Ethylammonium as an Alternative Cation for Efficient Perovskite Solar Cells from First-Principles Calculations. *RSC Adv.* **2019**, *9*, 7356–7361.

(43) Filipoiu, N.; Mitran, T. L.; Anghel, D. V.; Florea, M.; Pintilie, I.; Manolescu, A.; Nemnes, G. A. Investigation of Opto-Electronic Properties and Stability of Mixed-Cation Mixed-Halide Perovskite Materials with Machine-Learning Implementation. *Energies* **2021**, *14*, 5431.

(44) Huang, X.; Li, X.; Tao, Y.; Guo, S.; Gu, J.; Hong, H.; Yao, Y.; Guan, Y.; Gao, Y.; Li, C. et al. Understanding Electron-Phonon Interactions in 3D Lead Halide Perovskites from the Stereochemical Expression of $6s^2$ Lone Pairs. *J. Am. Chem. Soc.* **2022**,

(45) Im, J.-H.; Chung, J.; Kim, S.-J.; Park, N.-G. Synthesis, Structure, and Photovoltaic

Property of a Nanocrystalline 2H Perovskite-Type Novel Sensitizer ($CH_3CH_2NH_3$)PbI_3. *Nanoscale Res. Lett.* **2012**, *7*, 353.

(46) Lin, C.-W.; Liu, F.; Chen, T.-Y.; Lee, K.-H.; Chang, C.-K.; He, Y.; Leung, T. L.; Ng, A. M. C.; Hsu, C.-H.; Popović, J. et al. Structure-Dependent Photoluminescence in Low-Dimensional Ethylammonium, Propylammonium, and Butylammonium Lead Iodide Perovskites. *ACS Appl. Mater. Interfaces* **2020**, *12*, 5008–5016.

(47) Jung, M.-H. Exploration of Two-Dimensional Perovskites Incorporating Methylammonium for High Performance Solar Cells. *CrystEngComm* **2021**, *23*, 1181–1200.

(48) Onoda-Yamamuro, N.; Matsuo, T.; Suga, H. Calorimetric and IR Spectroscopic Studies of Phase Transitions in Methylammonium Trihalogenoplumbates (II). *J. Phys. Chem. Solids* **1990**, *51*, 1383–1395.

(49) Whitfield, P. S.; Herron, N.; Guise, W. E.; Page, K.; Cheng, Y. Q.; Milas, I.; Crawford, M. K. Structures, Phase Transitions and Tricritical Behavior of the Hybrid Perovskite Methyl Ammonium Lead Iodide. *Sci. Rep.* **2016**, *6*, 35685.

(50) Šimėnas, M.; Balčiūnas, S.; Mączka, M.; Banys, J.; Tornau, E. E. Exploring the Antipolar Nature of Methylammonium Lead Halides: A Monte Carlo and Pyrocurrent Study. *J. Phys. Chem. Lett.* **2017**, *8*, 4906–4911.

(51) Keshavarz, M.; Ottesen, M.; Wiedmann, S.; Wharmby, M.; Küchler, R.; Yuan, H.; Debroye, E.; Steele, J. A.; Martens, J.; Hussey, N. E. et al. Tracking Structural Phase Transitions in Lead-Halide Perovskites by Means of Thermal Expansion. *Adv. Mater.* **2019**, *31*, 1900521.

(52) Fateev, S. A.; Petrov, A. A.; Ordinartsev, A. A.; Grishko, A. Y.; Goodilin, E. A.; Tarasov, A. B. Universal Strategy of 3D and 2D Hybrid Perovskites Single Crystal Growth via In Situ Solvent Conversion. *Chem. Mater.* **2020**, *32*, 9805–9812.

(53) Banys, J.; Lapinskas, S.; Rudys, S.; Greicius, S.; Grigalaitis, R. High Frequency Measurements of Ferroelecrics and Related Materials in Coaxial Line. *Ferroelectrics* **2011**, *414*, 64–69.

(54) Svirskas, S.; Jablonskas, D.; Rudys, S.; Lapinskas, S.; Grigalaitis, R.; Banys, J. Broad-Band Measurements of Dielectric Permittivity in Coaxial Line Using Partially Filled Circular Waveguide. *Rev. Sci. Instrum.* **2020**, *91*, 035106.

(55) Kresse, G.; Furthmüller, J. Efficiency of ab-initio Total Energy Calculations for Metals and Semiconductors Using a Plane-Wave Basis Set. *Comput. Mater. Sci.* **1996**, *6*, 15–50.

(56) Kresse, G.; Joubert, D. From Ultrasoft Pseudopotentials to the Projector Augmented-Wave Method. *Phys. Rev. B* **1999**, *59*, 1758–1775.

(57) Perdew, J. P.; Ruzsinszky, A.; Csonka, G. I.; Vydrov, O. A.; Scuseria, G. E.; Constantin, L. A.; Zhou, X.; Burke, K. Restoring the Density-Gradient Expansion for Exchange in Solids and Surfaces. *Phys. Rev. Lett.* **2008**, *100*, 136406.

(58) Wang, Y.; Zhang, T.; Li, G.; Xu, F.; Wang, T.; Li, Y.; Yang, Y.; Zhao, Y. A Mixed-Cation Lead Iodide $MA_{1-x}EA_xPbI_3$ Absorber for Perovskite Solar Cells. *J. Energy Chem.* **2018**, *27*, 215–218.

(59) Nakada, K.; Matsumoto, Y.; Shimoi, Y.; Yamada, K.; Furukawa, Y. Temperature-Dependent Evolution of Raman Spectra of Methylammonium Lead Halide Perovskites, $CH_3NH_3PbX_3$ (X = I, Br). *Molecules* **2019**, *24*, 626.

(60) Maczka, M.; Zienkiewicz, J. A.; Ptak, M. Comparative Studies of Phonon Properties of Three-Dimensional Hybrid Organic-Inorganic Perovskites Comprising Methylhydrazinium, Methylammonium, and Formamidinium Cations. *J. Phys. Chem. C* **2022**, *126*, 4048–4056.

(61) Fabini, D. H.; Hogan, T.; Evans, H. A.; Stoumpos, C. C.; Kanatzidis, M. G.; Seshadri, R. Dielectric and Thermodynamic Signatures of Low-Temperature Glassy Dynamics in the Hybrid Perovskites $CH_3NH_3PbI_3$ and $HC(NH_2)_2PbI_3$. *J. Phys. Chem. Lett.* **2016**, *7*, 376–381.

(62) Govinda, S.; Kore, B. P.; Bokdam, M.; Mahale, P.; Kumar, A.; Pal, S.; Bhattacharyya, B.; Lahnsteiner, J.; Kresse, G.; Franchini, C. et al. Behavior of Methylammonium Dipoles in $MAPbX_3$ (X = Br and I). *J. Phys. Chem. Lett.* **2017**, *8*, 4113–4121.

(63) Cordero, F.; Craciun, F.; Trequattrini, F.; Imperatori, P.; Paoletti, A. M.; Pennesi, G. Competition between Polar and Antiferrodistortive Modes and Correlated Dynamics of the Methylammonium Molecules in $MAPbI_3$ from Anelastic and Dielectric Measurements. *J. Phys. Chem. Lett.* **2018**, *9*, 4401–4406.

(64) Svirskas, S.; Balčiūnas, S.; Šimėnas, M.; Usevicius, G.; Kinka, M.; Velicka, M.; Kubicki, D.; Castillo, M. E.; Karabanov, A.; Shvartsman, V. V. et al. Phase Transitions, Screening and Dielectric Response of $CsPbBr_3$. *J. Mater. Chem. A* **2020**, *8*, 14015–14022.

(65) Poglitsch, A.; Weber, D. Dynamic Disorder in Methylammoniumtrihalogenoplumbates (II) Observed by Millimeter-Wave Spectroscopy. *J. Chem. Phys.* **1987**, *87*, 6373–6378.

(66) Höchli, U.; Knorr, K.; Loidl, A. Orientational Glasses. *Adv. Phys.* **1990**, *39*, 405–615.

(67) Loidl, A.; Hemberger, J.; Winterlich, M.; Ries, H.; Böhmer, R. Linear and Nonlinear Dielectric Spectroscopy in Dipolar Glasses. *Ferroelectrics* **1996**, *176*, 43–59.

(68) Bokov, A. A.; Ye, Z.-G. Recent Progress in Relaxor Ferroelectrics with Perovskite Structure. *J. Mater. Sci.* **2006**, *41*, 31–52.

(69) Kleemann, W. Relaxor Ferroelectrics: Cluster Glass Ground State via Random Fields and Random Bonds. *Phys. Status Solidi (b)* **2014**, *251*, 1993–2002.

(70) Xu, Q.; Eguchi, T.; Nakayama, H.; Nakamura, N.; Kishita, M. Molecular Motions and Phase Transitions in Solid $CH_3NH_3PbX_3$ (X = C1, Br, I) as Studied by NMR and NQR. *Z. Naturforsch. A* **1991**, *46*, 240–246.

(71) Fabini, D. H.; Seshadri, R.; Kanatzidis, M. G. The Underappreciated Lone Pair in Halide Perovskites Underpins Their Unusual Properties. *MRS Bull.* **2020**, *45*, 467–477.

(72) Xing, G.; Mathews, N.; Lim, S. S.; Yantara, N.; Liu, X.; Sabba, D.; Grätzel, M.; Mhaisalkar, S.; Sum, T. C. Low-Temperature Solution-Processed Wavelength-Tunable Perovskites for Lasing. *Nat. Mater.* **2014**, *13*, 476–480.

(73) Fang, H.-H.; Raissa, R.; Abdu-Aguye, M.; Adjokatse, S.; Blake, G. R.; Even, J.; Loi, M. A. Photophysics of Organic-Inorganic Hybrid Lead Iodide Perovskite Single Crystals. *Adv. Funct. Mater.* **2015**, *25*, 2378–2385.

Graphical TOC Entry

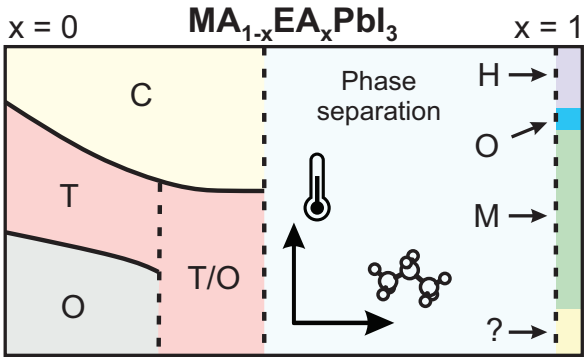

Supporting Information

Mixology of $MA_{1-x}EA_xPbI_3$ Hybrid Perovskites: Phase Transitions, Cation Dynamics and Photoluminescence

Mantas Šimėnas,* Sergejus Balčiūnas, Anna Gągor, Agnieszka Pieniążek, Kasper Tolborg, Martynas Kinka, Vytautas Klimavicius, Šarūnas Svirskas, Vidmantas Kalendra, Maciej Ptak, Daria Szewczyk, Artur Herman, Robert Kudrawiec, Adam Sieradzki, Robertas Grigalaitis, Aron Walsh, Mirosław Mączka, and Jūras Banys

E-mail: mantas.simenas@ff.vu.lt

Additional Experimental Data

^{1}H NMR spectroscopy data

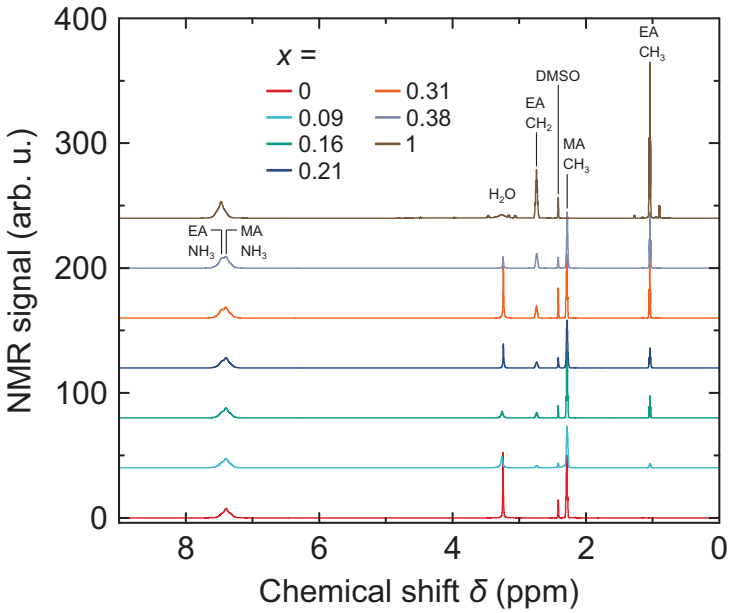

Figure S1: Stacked room temperature ^{1}H NMR spectra of $MA_{1-x}EA_xPbI_3$ used to determine the fraction of the EA cations in the synthesized compounds. The spectra for $x < 1$ are normalized to the MA cation methyl group signal. The signal assignment is based on the NMR COSY spectrum (see Figure S2).

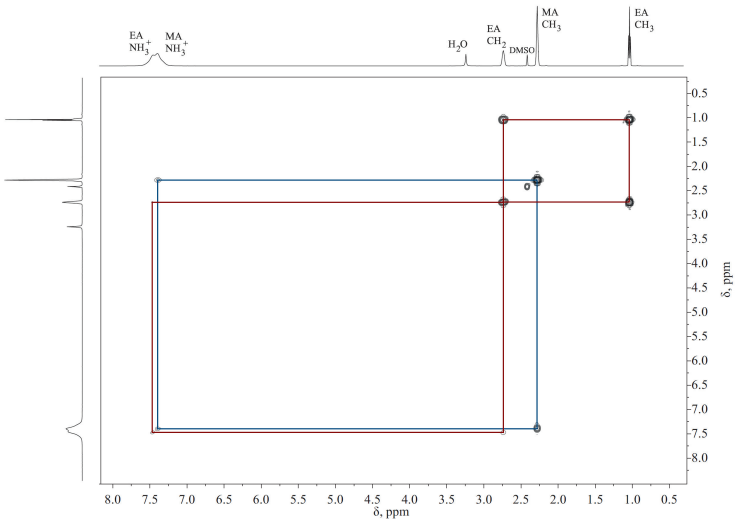

Figure S2: Room temperature ^{1}H NMR COSY spectrum of $MA_{0.62}EA_{0.38}PbI_3$. The cross peaks confirm our assignment of the ^{1}H NMR signals.

Raman spectroscopy data

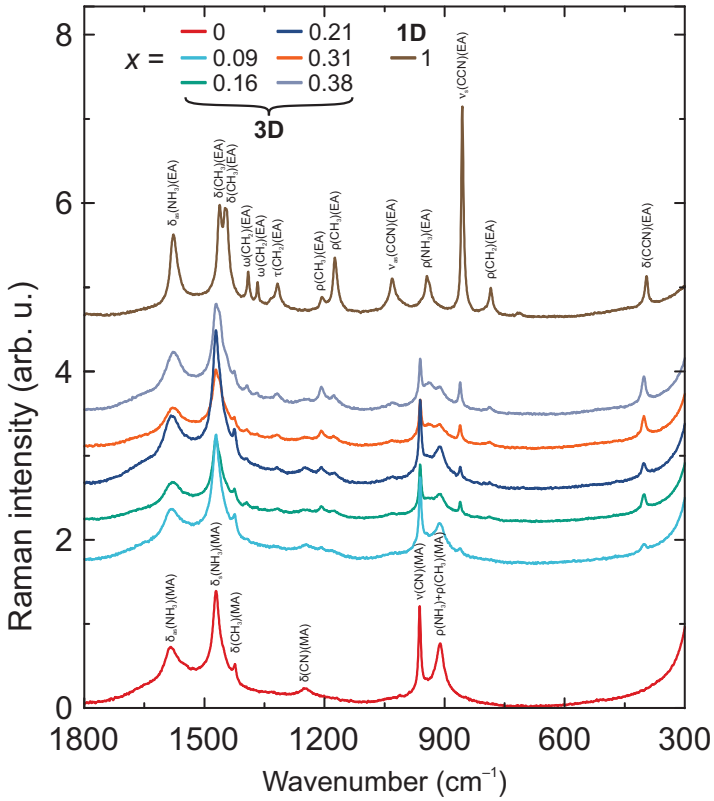

Figure S3: Stacked room temperature Raman spectra of $MA_{1-x}EA_xPbI_3$ with the corresponding assignment of the molecular vibrations based on the previous studies.[1,2]

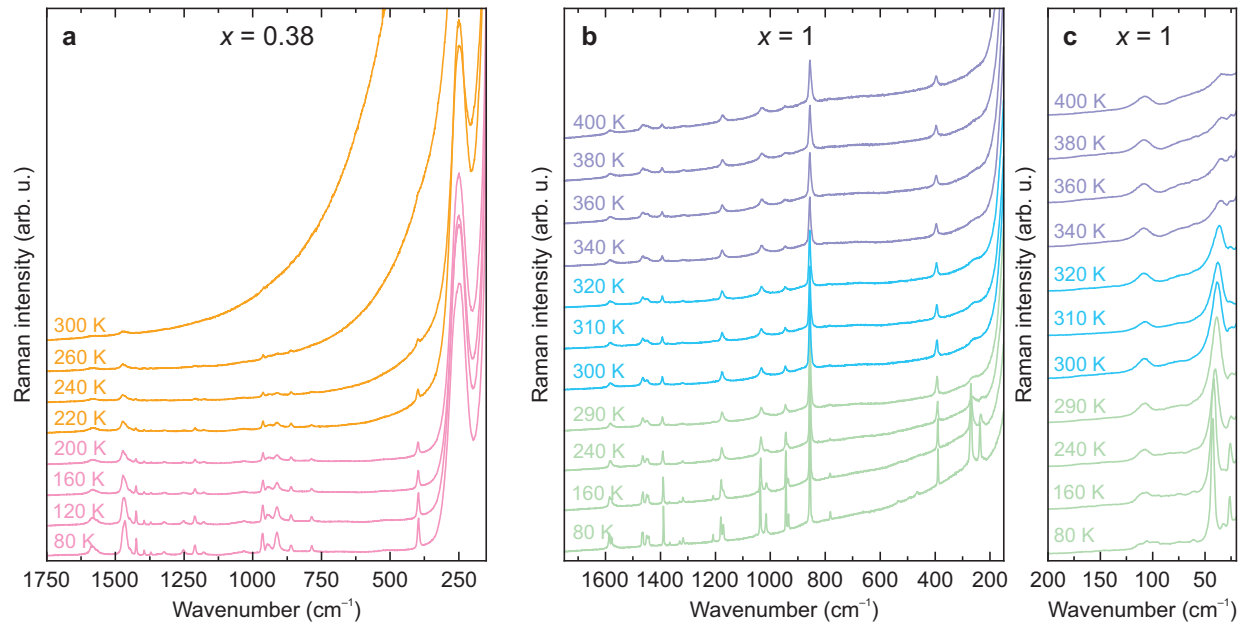

Figure S4: Temperature-dependent Raman spectra of the (a) $x = 0.38$ sample measured in the 1750−200 cm^{-1} range compared to the $x = 1$ sample measured in the (b) 1750−150 cm^{-1} and (c) 200 − 20 cm^{-1} ranges.

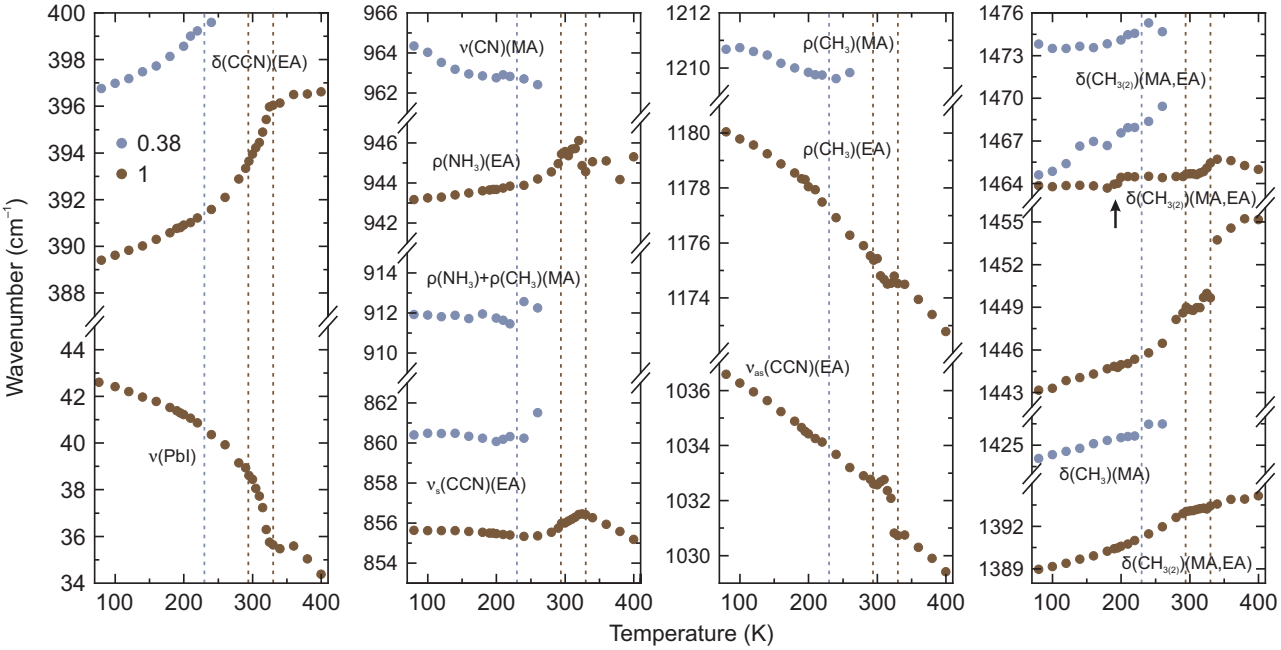

Figure S5: Thermal evolution of selected Raman bands for the $x = 0.38$ and $x = 1$ samples. The vertical lines correspond to temperatures of the phase transitions, while the arrow indicates the most pronounced anomaly due to the isostructural transition of $EAPbI_3$.

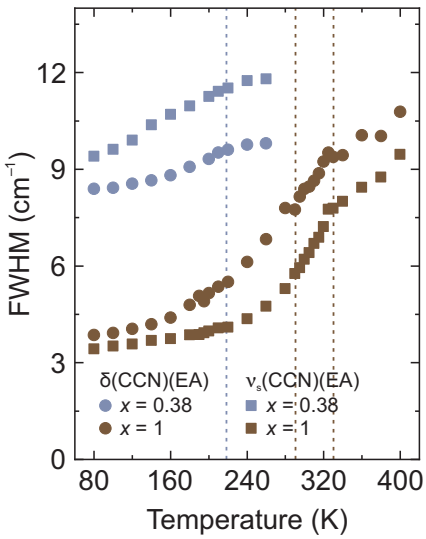

Figure S6: Temperature dependence of the selected Raman bandwidths of the $x = 0.38$ and $x = 1$ samples. Significantly wider Raman bands of the mixed compound compared to $EAPbI_3$ indicate presence of disorder at low temperature. The vertical lines correspond to temperatures of the phase transitions.

Powder XRD data

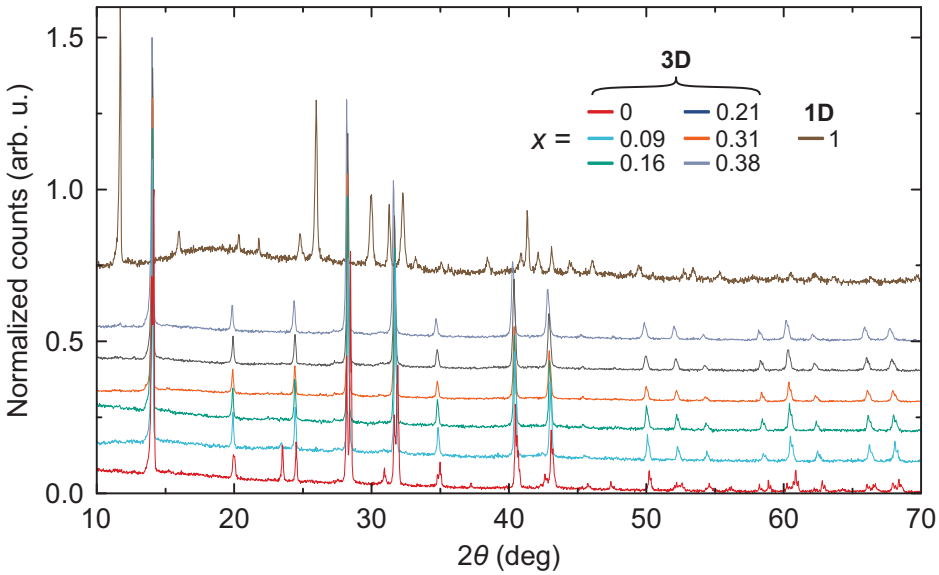

Figure S7: Stacked room temperature powder XRD patterns of $MA_{1-x}EA_xPbI_3$.

Ultrasonic data

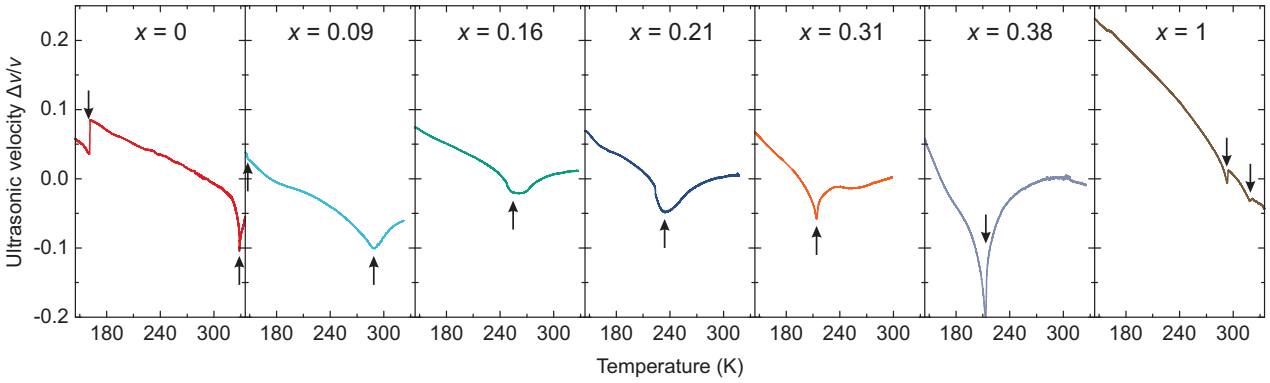

Figure S8: Temperature dependence of the ultrasonic velocity of $MA_{1-x}EA_xPbI_3$ single crystal samples. The change of the ultrasonic velocity is normalized to the room temperature value. The arrows indicate phase transition anomalies.

Single crystal XRD

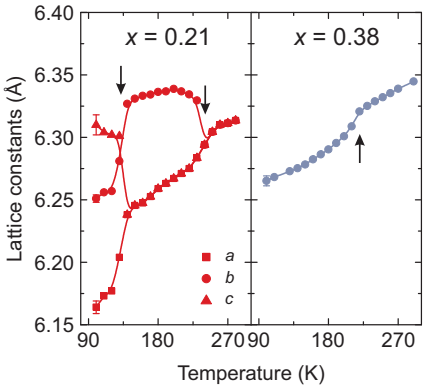

Figure S9: Temperature dependence of the lattice parameters of $MA_{1-x}EA_xPbI_3$ ($x = 0.21$ and 0.38) single crystal samples. The arrows indicate phase transition anomalies. A pseudo cubic model was used to refine the structures of $x = 0.38$ composition. The error bars are indicated on the lowest temperature points.

Reciprocal space reconstructions for $x = 0.21$ and $x = 0.38$ samples are presnted in Figure S10. The obtained diffraction patterns for the $x = 0.21$ sample are characteristic of tetragonal I-centered and primitive orthorhombic P lattice at 175 K and 110 K, respectively. They fit the phase diagram of $MAPbI_3$, where the symmetry reduction from $Pm\bar{3}m$ to $I4/mcm$, and to $Pnma$ is observed.[3] For the $x = 0.38$ sample, the diffraction picture is different. The patterns at 170 K do not fit the I-centered unit cell, whereas those at 120 K still resemble pseudo-merohedral twins, which in $MAPbI_3$ are present in the tetragonal phase. Therefore, a likely scenario is the formation of a new, tetragonal, or pseudo-tetragonal low-temperature phase for the highest concentration of EA in $MA_{1-x}EA_xPbI_3$ system.

Table S1 presents the crystal data, data collection and refinement results of the hexagonal and monoclinic structures of $EAPbI_3$. The detailed structural information is given in crystallographic information files (cif files) deposited in CCDC database with deposition numbers 2189712 and 2189713.

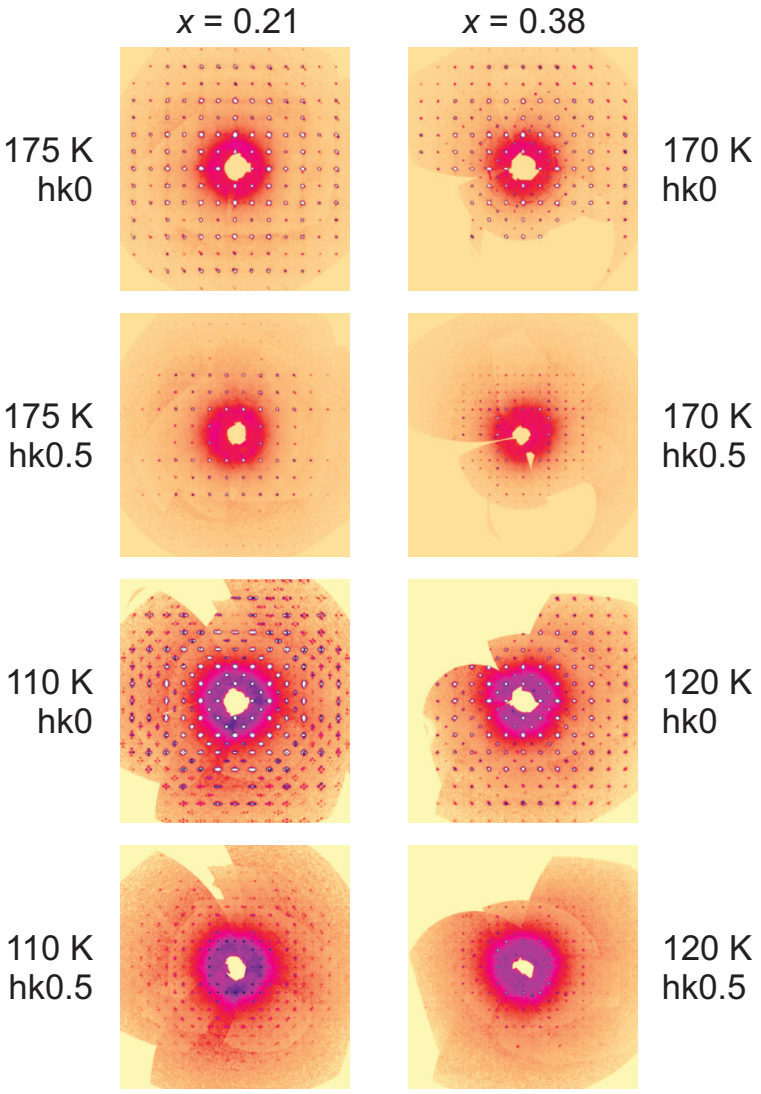

Figure S10: Reciprocal space reconstructions for $x = 0.21$ and $x = 0.38$ samples at different temperature. The Miller indexes are set according to the high-temperature cubic phase.

Table S1: Crystal data, data collection and refinement results of the hexagonal and monoclinic structures of $EAPbI_3$

	Phase I	**Phase III**
Crystal data		
Chemical formula	$I_3Pb \cdot C_2H_8N$	$I_3Pb \cdot C_2H_8N$
M_r	633.98	633.98
Crystal system, space group	Hexagonal, $P6_3/mmc$	Monoclinic, $P2_1/c$
Temperature (K)	340	120
a, b, c (Å)	8.8310(9), 8.8310(9), 8.0694(11)	8.5854(7), 14.7501(15), 8.1378(9)
α, β, γ (°)	90, 90, 120	90, 93.716(9), 90
V (Å^3)	544.99(13)	1028.37(18)
Z	2	4
μ (mm^{-1})	23.90	25.34
Crystal size (mm)	0.18 × 0.12 × 0.07	0.18 × 0.12 × 0.07
Data collection		
T_{min}, T_{max}	0.398, 1.000	0.692, 1.000
No. of measured, independent and observed $[I > 2\sigma(I)]$ reflections	4131, 311, 249	4044, 4044, 3480
R_{int}	0.030	-
$(\sin\theta/\lambda)_{max}$ (Å^{-1})	0.692	0.689
Refinement		
$R[F^2 > 2\sigma(F^2)], wR(F^2), S$	0.036, 0.102, 1.16	0.037, 0.099, 1.04
No. of reflections	311	4044
No. of parameters	11	67
No. of restraints	2	0
H-atom treatment	–	H-atom parameters constrained
$\Delta >_{max}, \Delta >_{min}$ (e Å^{-3})	0.76, -1.12	3.44, -3.47

Computer programs: CrysAlis PRO 1.171.38.41 (Rigaku OD), SHELXT 2014/5,[4] SHELXL 2018/3,[5] Olex2 1.5.[6]

Additional dielectric spectroscopy data

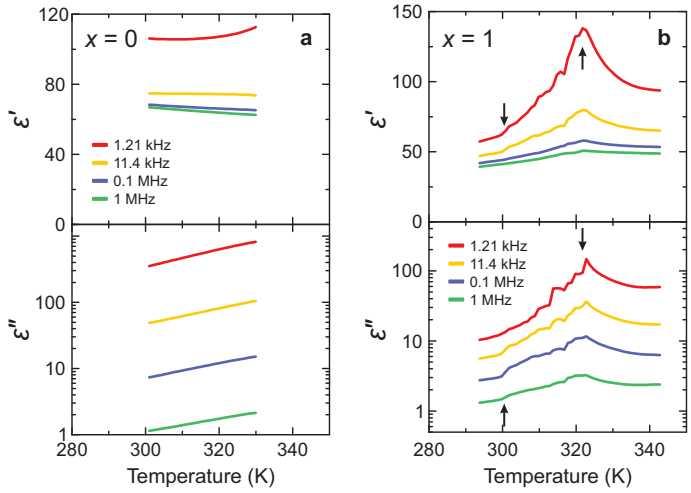

Figure S11: Temperature dependence of the complex dielectric permittivity of (a) $MAPbI_3$ and (b) $EAPbI_3$ single crystals in the high temperature region obtained on heating. The arrows mark the phase transition anomalies. The cubic-tetragonal phase transition of $MAPbI_3$ is not resolved in the dielectric data.

The frequency dependences of ε^* of $MA_{1-x}EA_xPbI_3$ compounds ($x = 0.21$, 0.31 and 0.38) are presented in Figure S12 for selected temperatures. The observed relaxations correspond to the main MA cation dynamics (τ_1 ($x = 0.21$) and τ_2 ($x = 0.31$ and 0.38) process). The relaxations were approximated using a Cole-Cole equation:[7]

$$\varepsilon^*(\omega) = \varepsilon(\infty) + \frac{\Delta\varepsilon}{1 + (i\omega\tau)^{1-\alpha}}. \tag{S1}$$

Here $\varepsilon(\infty)$ is the dielectric permittivity in the high-frequency limit, $\Delta\varepsilon$ denotes the dielectric strength of the process, τ is the mean relaxation time, and $\omega = 2\pi\nu$ is the angular measurement frequency. The relaxation width is described the parameter $0 \leq \alpha < 1$. For $\alpha = 0$, the Cole-Cole process reduces to the Debye relaxation, which describes non-interacting electric dipoles.

The best fits of Eq. S1 to the frequency domain data are also presented in Figure S12. For $x = 0.21$, the determined value of α at 110 K is around 0.53(1), while it increases to 0.80(1) for the $x = 0.38$ sample indicating much broader relaxation for the highly mixed

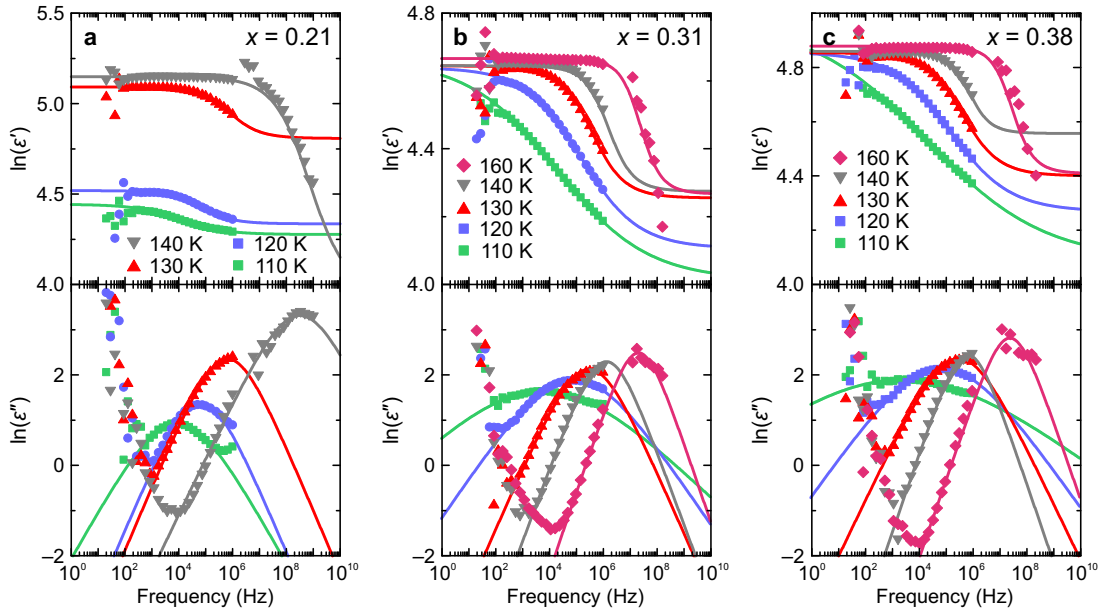

Figure S12: Frequency dependence of the complex dielectric permittivity of $MA_{1-x}EA_xPbI_3$ ($x = 0.21$, 0.31 and 0.38) single crystal compounds presented at selected temperatures. The solid curves are the best fits to a single Cole-Cole relaxation process.

compound.

The obtained temperature dependences of the mean relaxation times τ of all observed processes are presented in Figure S13. For all studied compounds, the relaxation times follow the Arrhenius law: $\tau = \tau_0 \exp(E_a/kT)$, where E_a and τ_0 denote the activation energy and attempt time, respectively, and k is the Boltzmann constant. The determined activation energies are also presented in Figure S13.

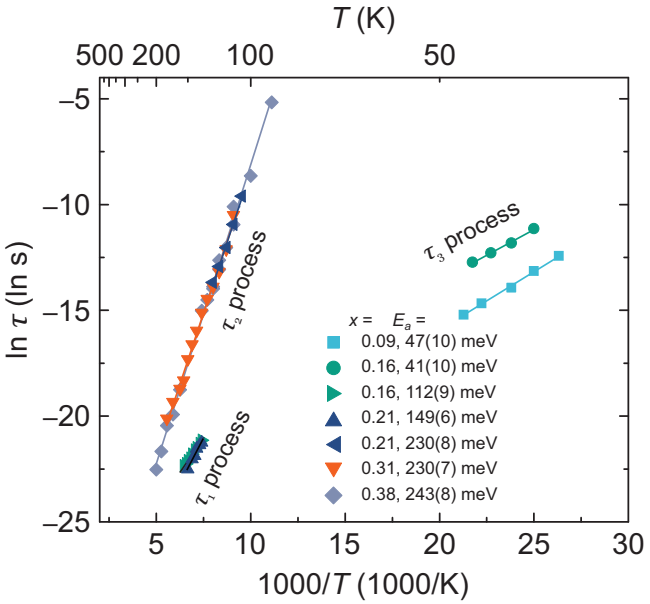

Figure S13: Inverse temperature dependence of the mean relaxation time of different processes observed in $MA_{1-x}EA_xPbI_3$ compounds measured by the broadband dielectric spectroscopy. The solid curves indicate fits to the Arrhenius equation.

Additional DFT data

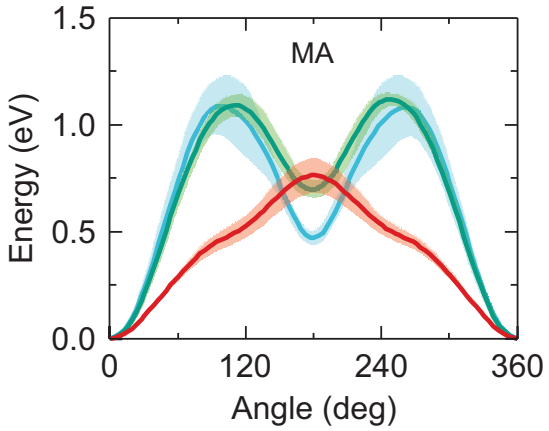

Figure S14: Averaged rotation barriers of the MA cations in $MA_{0.875}EA_{0.125}PbI_3$ supercell calculated by the DFT. The shaded regions mark the standard deviation of the rotation barriers.

Additional photoluminescence data

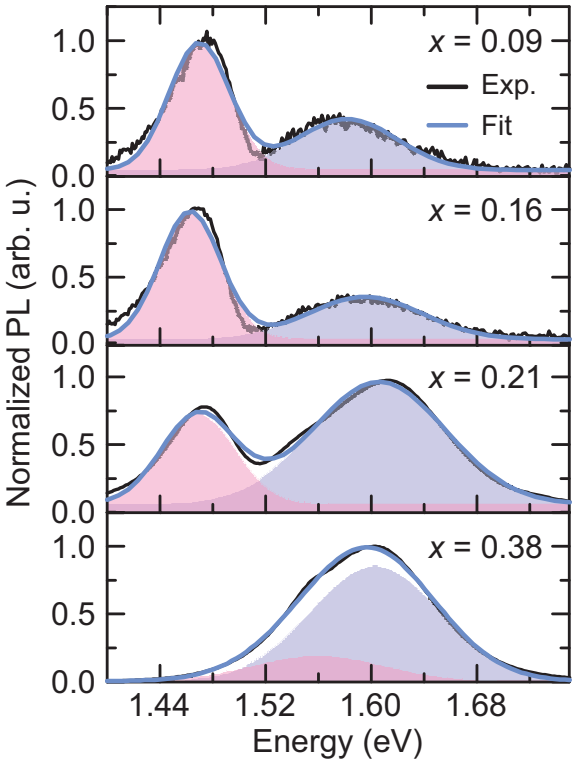

Figure S15: Normalized PL spectra of $MA_{1-x}EA_xPbI_3$ samples measured at 300 K and fitted by two Gaussian peaks: the high energy peak is attributed to free exciton emission, while the low energy peak may be attributed to bound excitons.

References

(1) Zeroka, D.; Jensen, J. O.; Samuels, A. C. Infrared Spectra of Some Isotopomers of Ethylamine and the Ethylammonium Ion: a Theoretical Study. *J. Mol. Struct.: THEOCHEM* **1999**, *465*, 119–139.

(2) Ptak, M.; Mączka, M.; Gagor, A.; Sieradzki, A.; Stroppa, A.; Di Sante, D.; Perez-Mato, J. M.; Macalik, L. Experimental and Theoretical Studies of Structural Phase Transition in a Novel Polar Perovskite-Like $[C_2H_5NH_3][Na_{0.5}Fe_{0.5}(HCOO)_3]$ Formate. *Dalton Trans.* **2016**, *45*, 2574–2583.

(3) Whitfield, P. S.; Herron, N.; Guise, W. E.; Page, K.; Cheng, Y. Q.; Milas, I.; Crawford, M. K. Structures, Phase Transitions and Tricritical Behavior of the Hybrid Perovskite Methyl Ammonium Lead Iodide. *Sci. Rep.* **2016**, *6*, 35685.

(4) Sheldrick, G. M. *SHELXT* – Integrated Space-Group and Crystal-Structure Determination. *Acta Crystallogr. A* **2015**, *71*, 3–8.

(5) Sheldrick, G. M. Crystal Structure Refinement with *SHELXL*. *Acta Crystallogr. C* **2015**, *71*, 3–8.

(6) Dolomanov, O. V.; Bourhis, L. J.; Gildea, R. J.; Howard, J. A. K.; Puschmann, H. *OLEX2*: a Complete Structure Solution, Refinement and Analysis Program. *J. Appl. Crystallogr.* **2009**, *42*, 339–341.

(7) Schonhals, A.; Kremer, F. *Broadband Dielectric Spectroscopy*, 1st ed.; Springer-Verlag Berlin Heidelberg, 2003.